OPTICS

# Higher-order topological polariton corner state lasing

Jinqi Wu[1]†, Sanjib Ghosh[2]†, Yusong Gan[3], Ying Shi[3], Subhaskar Mandal[1], Handong Sun[1], Baile Zhang[1], Timothy C. H. Liew[1,4]*, Rui Su[1,4,5]*, Qihua Xiong[2,3,6,7]*



**Unlike conventional laser, the topological laser is able to emit coherent light robustly against disorders and defects because of its nontrivial band topology. As a promising platform for low-power consumption, exciton polariton topological lasers require no population inversion, a unique property that can be attributed to the part-light-part-matter bosonic nature and strong nonlinearity of exciton polaritons. Recently, the discovery of higher-order topology has shifted the paradigm of topological physics to topological states at boundaries of boundaries, such as corners. However, such topological corner states have never been realized in the exciton polariton system yet. Here, on the basis of an extended two-dimensional Su-Schrieffer-Heeger lattice model, we experimentally demonstrate the topological corner states of perovskite polaritons and achieved polariton corner state lasing with a low threshold (approximately microjoule per square centimeter) at room temperature. The realization of such polariton corner states also provides a mechanism of polariton localization under topological protection, paving the way toward on-chip active polaritonics using higher-order topology.**



## INTRODUCTION

Topological insulators (TIs) are novel materials that are insulating in the bulk but conducting along their edges robustly against perturbations because of their nontrivial band topology (*1*, *2*). The concept of band topology can date back to the observation of the quantum Hall effect in 1980, where the quantized Hall conductance emerged in a two-dimensional (2D) electron gas as a result of topological edge states (*3*). Protected by the band topology, these topological edge states exhibit strong immunity against backscattering and disorder, rendering a promising prospect toward low-power consumption devices with robust performances (*1*, *2*). Similar concepts were later widely extended into various research areas for the advantage of topological protection including microwaves (*4*, *5*), acoustics (*6*, *7*), mechanics (*8*), and photonics (*9*, *10*). Particularly in photonics, the topological concept has not only played a crucial role in exploring novel phenomena, such as anomalous Floquet phases (*11*), photonic Weyl points (*12*), Fermi arcs (*13*), and non-Hermitian topology (*14*), but also essentially revolutionized the principle of guiding and confining photons for novel optical devices, including unidirectional waveguides (*15*), robust routers (*16*), and topological lasers (*17*).

In topological photonic devices, topological lasers represent a remarkable breakthrough that allows coherent light emission with robustness against perturbations, fabrication defects, and long-term degradation that limit the performance of the conventional laser (*18*–*20*). Most topological lasers rely on population inversion and demand laser threshold with relatively high-power consumption. Alternatively, by dressing matter excitations of excitons with photons, one can achieve hybrid bosonic quasiparticles of exciton polaritons in the strong coupling regime with combined advantages, serving as ideal candidates for topological lasers with low-power consumption (*21*–*23*). Compared with bare photonic systems, exciton polaritons have higher sensitivity to external stimuli, stronger nonlinearity, and stronger lasing gain because of their exciton component (*24*, *25*). Combined with their extremely low effective mass, exciton polaritons can macroscopically form collective polariton condensates through stimulated scattering, leading to coherent emission of polariton lasing with ultralow threshold (*26*–*28*). Meanwhile, benefitting from their photonic component, polaritons exhibit notable flexibility of confinement in microstructures that further enables distinct topological phases. By engineering the trapping potentials, topological polariton states and their lasing have been successfully achieved in various systems of GaAs (*21*, *22*), halide perovskites (*29*, *30*), and organics (*31*, *32*).

Recently, the discoveries of higher-order TIs (HOTIs) (*33*–*40*) have generalized band topology from first order to higher order (*1*). For instance, instead of hosting topological edge states propagating around edges, a 2D HOTI supports 0D topological states known as corner states that localize at the corners. Polaritonic corner states provide a topological mechanism of polariton localization, which can facilitate coherent and robust lasing, as well as supporting information storage and manipulation (*40*–*48*). While HOTIs have been realized in many other systems (*38*, *41*, *42*, *45*, *49*, *50*), there has been no realized higher-order topological phase in the exciton polariton system so far. In this study, we report the experimental demonstration of the higher-order topological polariton corner states and their low threshold lasing in a 2D lattice of coupled perovskite micropillars at room temperature.

## RESULTS

### Mechanism of the 2D perovskite lattice

We implement a 2D lattice to construct higher-order corner states, following an extended 2D Su-Schrieffer-Heeger (SSH) model from the 1D SSH lattice (*30*). As shown in Fig. 1A, a typical 1D SSH lattice

[1]Division of Physics and Applied Physics, School of Physical and Mathematical Sciences, Nanyang Technological University, 637371, Singapore. [2]Beijing Academy of Quantum Information Sciences, Beijing 100193, P.R. China. [3]State Key Laboratory of Low-Dimensional Quantum Physics and Department of Physics, Tsinghua University, Beijing 100084, China. [4]MajuLab, International Joint Research Unit UMI 3654, CNRS, Université Côte d'Azur, Sorbonne Université, National University of Singapore, Nanyang Technological University, Singapore. [5]School of Electrical and Electronic Engineering, Nanyang Technological University, 639798, Singapore. [6]Frontier Science Center for Quantum Information, Beijing 100084, P.R. China. [7]Collaborative Innovation Center of Quantum Matter, Beijing, P.R. China.
*Corresponding author. Email: qihua_xiong@tsinghua.edu.cn (Q.X.); surui@ntu.edu.sg (R.S.); timothyliew@ntu.edu.sg (T.C.H.L.)
†These authors contributed equally to this work.

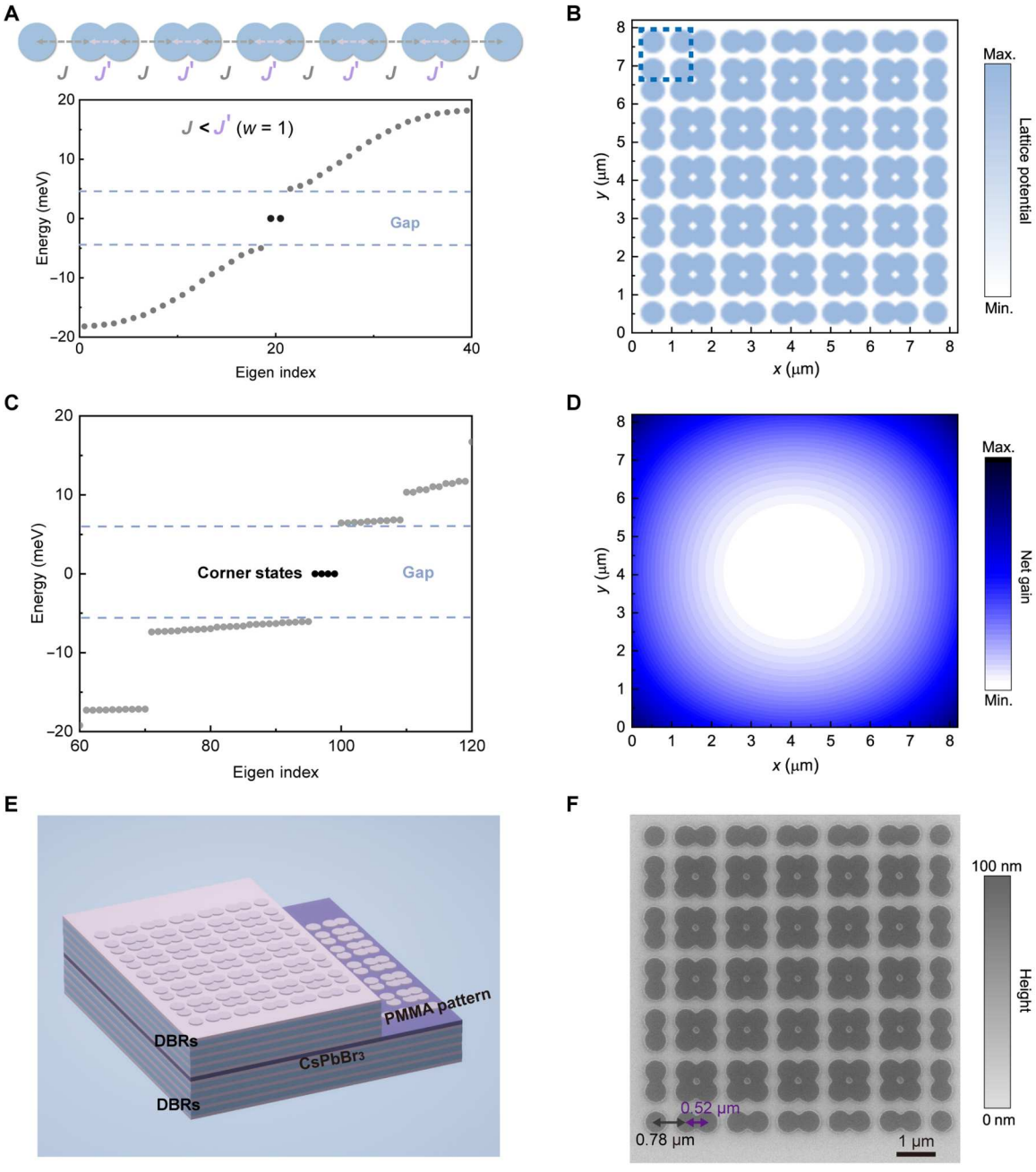


**Fig. 1. Design of the 2D perovskite lattice.** (**A**) Schematic diagram of a 1D SSH lattice with intracell hopping *J*, intercell hopping *J*′, and the relevant band structure of nontrivial (winding number $w = 1$) topological phase. (**B**) Schematic diagram of a 2D SSH lattice with lattice potential. The blue dashed lines highlight one unit cell composing of four identical pillars. These four pillars interact via the nearest-neighbor and the next-nearest-neighbor hopping. (**C**) Band structure of the extended 2D SSH lattice in (B). The corner states in the gap at $E = 0$ are highlighted in black. (**D**) Spatial profile of the gain concentrated at the corners of the polariton lattices. (**E**) Illustration of the 2D perovskite lattice embedded between distributed Bragg reflectors (DBRs), where the lattice pattern is created by patterning the poly(methyl methacrylate) (PMMA) spacer layer. (**F**) Scanning electron microscopy image of the 2D $CsPbBr_3$ perovskite lattice with a thickness around 100 nm, showing 12 × 12 pillars (6 × 6 unit cells) with a diameter of 0.65 μm connected with alternating interpillar distances of 0.78 and 0.52 μm along both *x* and *y* directions.

is formed by identical pillars spatially arranged with alternative intracell hopping strength *J* and intercell hopping strength *J*′. When the intercell hopping *J*′ is stronger than the intracell hopping *J*, the lattice supports a nontrivial ($w = 1$; here, *w* is the winding number) topological phase with two topological edge states in the gap. Our lattice is an extended 2D version of the 1D SSH lattice and consists of 6 × 6 unit cells with the nearest-neighbor and the next-nearest-neighbor hoppings terms. Each unit cell is composed of four identical pillars as shown in Fig. 1B. Note that a mere extension of the 1D SSH lattice with trivial nearest-neighbor hopping will support corner states without a gap, which can easily couple to bulk states (*50*). In our scheme, the next-nearest-neighbor hopping $J_{next}$ of

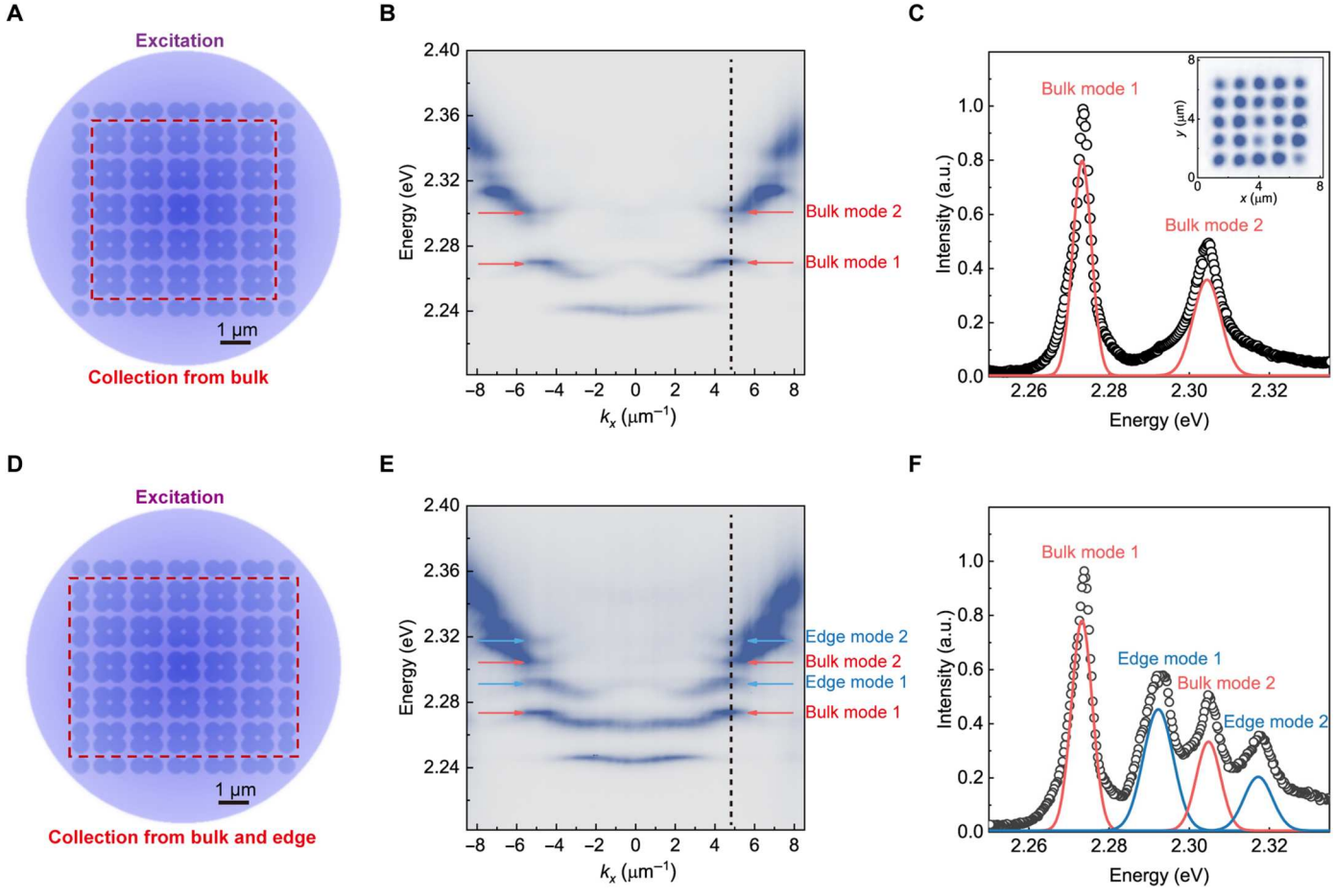


**Fig. 2. Characterization of bulk states and edge states in the 2D perovskite lattice at room temperature.** (**A**) Schematic of excitation of the whole micropillar lattice that is highlighted in the purple area. The emission is collected from the bulk area framed by the red dashed lines. (**B**) Momentum-space polariton energy dispersions of bulk area as indicated in (A). The dashed black line is at $k_x = 4.8$ μm$^{-1}$. The red arrows indicate the bulk states. (**C**) Polariton emission spectrum at $k_x = 4.8$ μm$^{-1}$ in (B) fitted with a Gaussian function, showing the large bulk bandgap of 31 meV. Inset: Real-space image of the perovskite lattice shows the emission of bulk states, corresponding to the bulk mode 1. (**D**) Schematic of excitation for whole micropillars highlighted in purple area and emission collected from bulk and two edges as framed by red dashed lines. (**E**) Momentum-space polariton energy dispersions of bulk and edge area labeled in (D). The red arrows and blue arrows represent the bulk states and edge states, respectively. (**F**) Polariton emission spectrum at the edge of the second Brillouin zone ($k_x = 4.8$ μm$^{-1}$) fitted with a Gaussian function. There are four peaks (bulk mode 1: 2.273 eV, edge mode 1: 2.292 eV, bulk mode 2: 2.304 eV, and edge mode 2: 2.317 eV) showing the energy splitting as large as 12 meV between edge mode 1 and bulk mode 2. a.u., arbitrary units.

exciton polaritons induces the topological gap opening for the nontrivial corner states (see the Supplementary Material for details). Similar mechanisms have been discussed in topological electrical circuits (*51*).

From the simulated band structure (Fig. 1C), four energy-degenerate corner states protected by a topological bandgap can be observed. The spatial profile of the gain concentrated at the four corners of the polariton lattices is shown in Fig. 1D. In experiments, we fabricate a 2D micropillar array within a cesium lead bromide ($CsPbBr_3$) perovskite microcavity (Materials and Methods). Specifically, the microcavity is formed by a bottom distributed Bragg reflector (DBR), a central perovskite ($CsPbBr_3$) crystalline layer, a lattice pattern of electron beam resist, and a top DBR (Fig. 1E). The lattice is created by patterning the spacer layer of poly(methyl methacrylate) (PMMA) by electron beam lithography (Materials and Methods) and is aligned with the crystal axes of the perovskite (fig. S4). As shown in a scanning electron microscopy image (Fig. 1F), the 2D micropillar array is formed by 12 × 12 identical coupled micropillars (6 × 6 unit cells) with a thickness of ~100 nm (fig. S5), a diameter of 0.65 μm, center-to-center distance of 0.78 μm within a unit cell, and a distance of 0.52 μm between unit cells. To our best knowledge, these are the smallest micropillars realized in any exciton polariton systems. The minimized size is a key parameter that helps to obtain large separation between different energy bands compared to the polariton linewidth.

## Characterization of bulk and edge states in the 2D perovskite lattice

To study the polariton bulk, edge, and corner states, the band structure of the 2D lattice is characterized by angle-resolved polariton energy dispersions in the linear (low-density) regime, under a nonresonant excitation with a continuous wave laser of 457 nm. The whole micropillar lattice is excited with a spot diameter of 15 μm while the area of emission collection is selected, as schematically

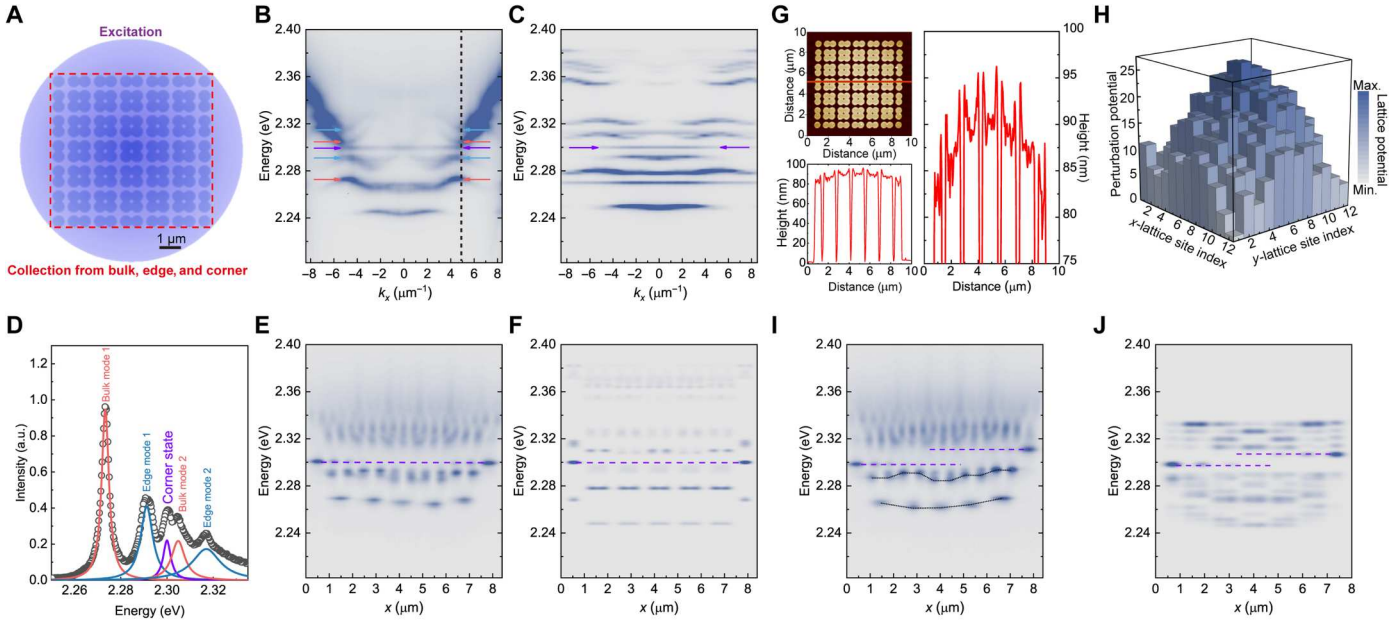


**Fig. 3. Topological corner states in the 2D perovskite lattice at room temperature.** (**A**) Schematic diagrams of excitation and emission collection from the whole 2D lattice. (**B** and **C**) Experimentally measured (B) and theoretically calculated (C) momentum-space polariton energy dispersions of the 2D perovskite lattice collected from the area framed by the red dashed lines. The black dashed line highlights the corner states in the gap. (**D**) Polariton emission spectrum of (B) at the edge of the second Brillouin zone ($k_x = 4.8$ μm$^{-1}$) fitted with a Gaussian function. The corner state of $E = 2.300$ eV locates in the gap splitting of 12 meV between edge mode 1 and bulk mode 2. (**E** and **F**) Experimentally measured (E) and theoretically calculated (F) energy-resolved spatial images, respectively. The purple dashed lines present the emission from degenerate corners. (**G**) Atomic force microscopy image (top left) of the inhomogeneous 2D perovskite lattice. The height profile (bottom left) of the inhomogeneous perovskite lattice along the red dashed line in the top left image. The magnified image (right) of the height profile in the bottom left image, showing the inhomogeneity of the lattices. (**H**) The simulated lattice potential perturbation on each lattice site. (**I** and **J**) With introducing the lattice potential perturbation, experimentally measured (I) and theoretically calculated (J) energy-resolved spatial images of the 2D perovskite lattice, respectively. The fitted black dotted lines notified the perturbation of the lattice potential. Two purple dashed lines show the corner emission with different energies (2.298 and 2.310 eV, respectively).

shown in Fig. 2 (A and D). We first characterize the polariton bulk states with the emission from the bulk area as schematically framed by the red dashed lines in Fig. 2A, which covers 5 × 5 unit cells. Figure 2B shows the angle-resolved photoluminescence of the bulk states selected in Fig. 2A, exhibiting several energy bands. Because of the minimized size of pillars, these energy bands mainly originate from the coupling of *s*-mode polaritons with cylindrical symmetry in the pillars. We observe a huge gap opening as large as 31 meV at $k_x = 4.8$ μm$^{-1}$ between the bulk 1 and bulk 2 bands, as shown in Fig. 2C. The inset of Fig. 2C presents the real-space image of the perovskite lattice measured at the energy of bulk mode 1 (2.273 eV, 545.5 nm), which shows the emission of bulk states corresponding to collection area framed by the red dashed lines in Fig. 2A. The slight inhomogeneity of real-space bulk emission in the inset is resulted from inhomogeneous energy distribution induced by the lattice fabrication.

To obtain the angle-resolved photoluminescence of the edge state, we collected the emission from both edge and bulk areas (framed by red dashed lines in Fig. 2D), which includes 10 × 12 single pillars. Compared with the bulk polariton dispersion shown in Fig. 2B, two additional sub-bands appear within the bulk bandgap as shown in Fig. 2E (blue arrows), which correspond to the dispersion of topological edge states. Figure 2F depicts the polariton photoluminescence at $k_x = 4.8$ μm$^{-1}$ (black dashed line in Fig. 2E), displaying the four peaks (bulk mode 1: 2.273 eV, edge mode 1: 2.292 eV, bulk mode 2: 2.304 eV, and edge mode 2: 2.317 eV) obtained by fitting with Gaussian functions. The gap opening between edge mode 1 and bulk mode 2 is as large as 12 meV, which gives the opportunity to sustain robust corner states.

## Topological corner states in the 2D perovskite lattice

To observe the topological corner states, we collect the emission from the entire 2D perovskite lattice consisting of the bulk, edge, and corners (red dashed lines in Fig. 3A) for probing the polariton band structure. As shown in Fig. 3B, the experimental momentum-space polariton energy dispersion of the entire lattice exhibits similar bands as in Fig. 2E but with an additional discrete state, which agrees with the theoretical calculation of polariton lattice dispersion in Fig. 3C. We further extract the energy spectrum in the gap at $k_x = 4.8$ μm$^{-1}$ by fitting with a Gaussian function as shown in Fig. 3D; the discrete emission located at $E = 2.300$ eV between the bulk band and edge band corresponds to the topological corner state. It can be further confirmed from the energy-resolved spatial image in Fig. 3E, where the discrete state exhibits strong localization at the corner sites and is in good agreement with the theoretical calculations (Fig. 3F).

We then introduce the onsite lattice energy perturbation by varying the thickness of pattern in another sample. Specifically, the height profile, corresponding to the red dashed line tracked in the atomic force microscopic image (top left of Fig. 3G) of the 2D perovskite lattice, displays the inhomogeneous thickness of the pattern ranging between 80 and 97 nm. Because of the thickness

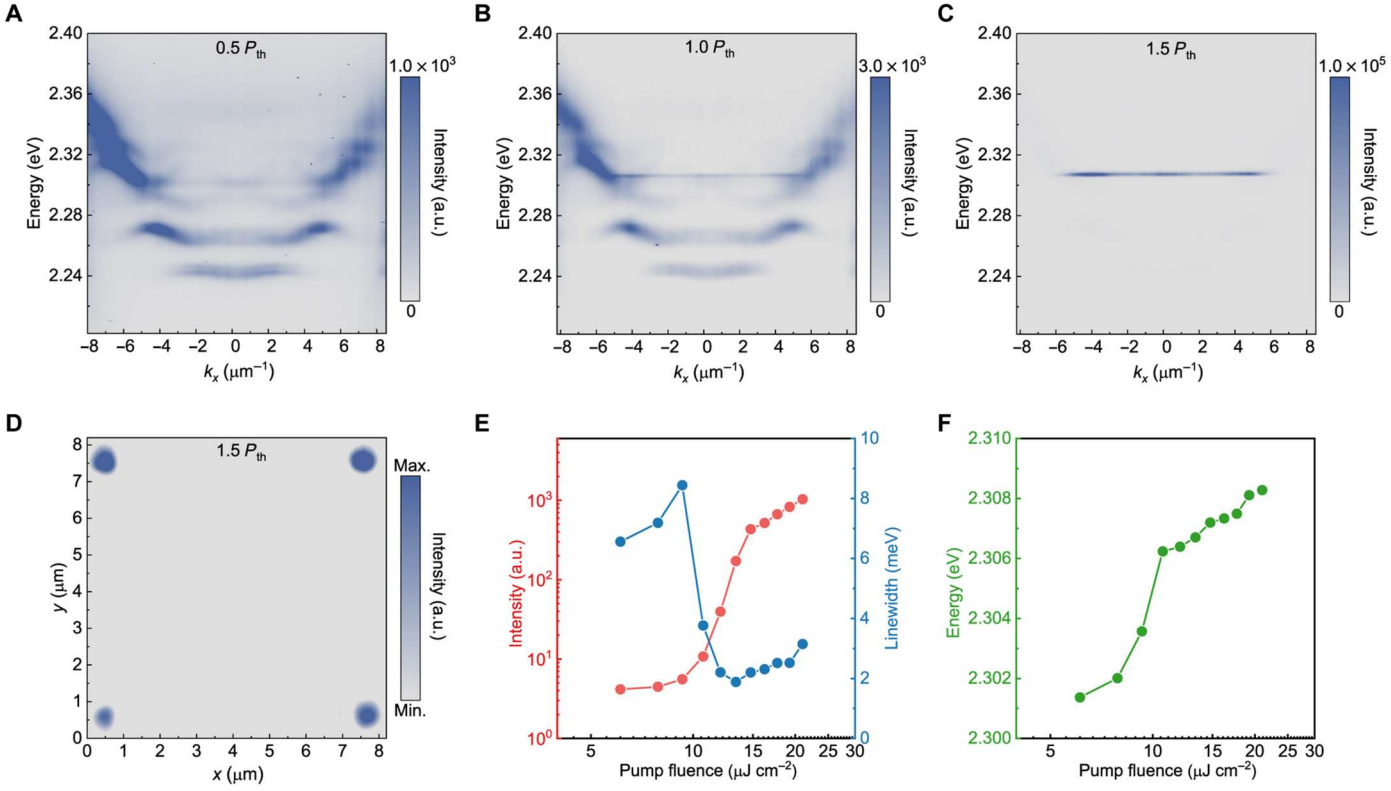


**Fig. 4. Exciton polariton condensation into corner states at room temperature.** (**A** to **C**) Momentum-space polariton energy dispersions of the 2D perovskite lattice with the increase of the excitation power at $P = 0.5\ P_{th}$ (A), $P = 1.0\ P_{th}$ (B), $P = 1.5\ P_{th}$ (C), respectively. (**D**) Experimental real-space image of polariton lasing at corner states at $P = 1.5\ P_{th}$. (**E**) The integrated intensity and linewidth of the corner states as a function of pump fluence, showing the increasing of intensity by three orders and narrowing of linewidth at a threshold of $P_{th} = 10\ \mu J.cm^{-2}$. (**F**) Emission energy of the corner states as a function of pump fluence, which exhibits a continuous blueshift trend because of the repulsive interactions.

variation caused during the fabrication process, the topological lattice described by the Hamiltonian $H$ (see the Supplementary Materials) is perturbed by an effective on-site inhomogeneous potential. By fitting the experimentally measured dispersion of the perturbed lattice, we numerically extract the corresponding perturbating potential (see Fig. 3H). From the experimental (Fig. 3I) and theoretical (Fig. 3J) energy-resolved spatial images, we can see the robust existence of corner states in the topological bandgap, even in presence of the fluctuation of lattice potentials as large as 20 meV. Because of the perturbation, the degeneracy of the corner states is lifted, and they appear with different energies (2.298 and 2.310 eV, respectively) within the topological bandgap.

## Exciton polariton condensation into corner states

The polariton lattice is excited by a pulsed laser of 400 nm with a spot diameter of 18 μm to reach the nonlinear regime of topological corner states. At the low excitation power of $0.5\ P_{th}$ ($P_{th}$ is threshold pump fluence), the distinct features of the 2D lattice band structure are presented in the polariton dispersion (Fig. 4A), which is consistent with Fig. 3C. Typically, in the system without topological structure design, the polaritons intend to condense at the ground state. However, in our 2D HOTI polariton system, with the increase of excitation power, the polariton density is enhanced in the corner state (Fig. 4B) and triggered by the stimulated scattering at $P = P_{th}$, where a large fraction of polaritons starts to accumulate. Last, from both energy-resolved momentum space (Fig. 4C) and energy-resolved spatial imaging (fig. S7A) at $P = 1.5\ P_{th}$, the polariton condensation is observed in the corner states at the energy of 2.307 eV with maximum gain. Simultaneously, as shown in Fig. 4D at $P = 1.5\ P_{th}$, the real-space image displays the polariton lasing localized at the four topological corner states, which is in agreement with the theoretical calculation shown in fig. S7B. Here, because the pump laser has a large spot size with a diameter of 18 μm that covers the whole micropillar lattice, all four corner modes are excited with polariton lasing. In principle, the four corner states are spatially separated, and the selective excitation of each individual corner state can be achieved with a minimized pump spot at specified corner location. To further quantify the occurrence of topological corner state lasing, we extract the integrated intensity, linewidth, and blueshift of corner states from the power-dependent polariton energy dispersions at $k_x = 4.8\ \mu m^{-1}$. The integrated intensity, as shown in Fig. 4E, increases rapidly by three orders of magnitude at a threshold of $P_{th} = 10\ \mu J\ cm^{-2}$. Meanwhile, Fig. 4E exhibits sharp narrowing of the linewidth from 9 to 2 meV at $P = P_{th}$, signifying the spontaneous buildup of temporal coherence in the polariton condensation regime. In addition, because of the repulsive nonlinear polariton interactions, there is a blueshift of polariton emission energy with the increase of excitation pump fluence in Fig. 4F. All the above characteristics serve as signatures of polariton lasing into the corner states.

## DISCUSSION

We have demonstrated low-threshold topological polariton lasing in corner states at room temperature in halide perovskite microcavity systems. By implementing the extended 2D SSH lattice of coupled perovskite micropillars, our work represents the first realization of higher-order topology in polariton system, where detailed characterization of topological corner states has been performed in comparison with the bulk and edge states. In addition, we have realized exciton polariton condensation in topological corner states with a low threshold at room temperature. Our work extends the scope of higher-order topology to polariton systems and provide a promising platform for topological on-chip lasing.

## MATERIALS AND METHODS

### Two-dimensional perovskite lattice microcavity fabrication

The microcavity is formed by bottom DBRs, a central perovskite ($CsPbBr_3$), a PMMA lattice pattern, and a top DBR. In detail, the bottom DBR is composed of 30.5 pairs of $TiO_2/SiO_2$ deposited using an electron beam evaporator. $CsPbBr_3$ is tape-transferred to the bottom DBRs, after single-crystal $CsPbBr_3$ is grown on mica via chemical vapor deposition as described in our previous reports (*52*). Next, a PMMA layer is spin-coated on the $CsPbBr_3$ and subsequently patterned by electron beam lithography. Last, the top DBRs consisting of 7.5 pairs of $TiO_2/SiO_2$ are deposited on that using the E-beam evaporator.

### Optical spectroscopy characterizations

The momentum-space and real-space photoluminescence spectra and the energy-resolved spatial image are measured by a home-built angle-resolved photoluminescence setup with Fourier transform optics. After the excitation on perovskite microcavity, the signal emission is collected through a ×50 microscope objective (numerical aperture: 0.75) and detected using a 550-mm focal length spectrometer (Horiba iHR550) with a grating (600 lines/mm) and liquid nitrogen–cooled charge-coupled device camera (256 pixels by 1024 pixels). Considering the detection of different polariton states, the different emission areas are selected by the spatial filter in the real-space plane. Regarding the excitation source, in the linear regime, the microcavity is pumped using a continuous wave laser (wavelength: 457 nm) with a pump spot diameter of ~15 μm, while in the nonlinear regime, the microcavity is excited using a pulsed laser (wavelength: 400 nm, duration: 1 kHz, pulse width: 100 fs) with a homogeneous pump spot diameter of ~18 μm.

### Theoretical calculations

Our theoretical description of microcavity exciton polaritons is based on Schrodinger's equation. In our perovskite microcavity, photons show strong polarization-dependent anisotropy. We describe the effective perovskite anisotropy with anisotropic effective photonic masses along $x$ and $y$ axes for a given linear polarization component. The considered Schrodinger's equation is given by

$$i\hbar\dot{\Psi}_S(\vec{r},t) = \left[\frac{\Delta_S}{2} - \frac{\hbar^2}{2m_S^x}\frac{\partial^2}{\partial x^2} - \frac{\hbar^2}{2m_S^y}\frac{\partial^2}{\partial y^2} + V_{\mathrm{Latt}}(\vec{r})\right]\Psi_S(\vec{r},t) + \frac{g_0}{2}\Phi(\vec{r},t)$$

where $\Psi_S(\vec{r},t)$ and $\Phi(\vec{r},t)$ are the photonic and excitonic wave functions, respectively. The index $S = X, Y$ indicates the linear polarization direction; $\Delta_S$ and $m_S^{x,y}$ are the polarization-dependent energy shift and effective photon masses, respectively; and $g_0$ is the Rabi energy splitting. The potential function $V_{\mathrm{Latt}}(\vec{r})$ represents the 2D lattice supporting the topological corner states. The excitonic wave function $\Phi(\vec{r},t)$ also satisfies the effective Schrodinger equation

$$i\hbar\dot{\Phi}(\vec{r},t) = E_{\mathrm{ex}}\ \Phi(\vec{r},t) + \frac{g_0}{2}\Psi_S(\vec{r},t)$$

The solutions to these coupled equations can be obtained with the exact diagonalization, where eigenvalues $\{E_n\}$ and eigenvectors $\{(\psi_n, \phi_n)\}$ of the Hamiltonian are calculated to obtain different properties of the system. The dispersion figure given by the energy-resolved intensity in the momentum space is obtained from

$$I_M(E,k) = \frac{1}{\pi\sigma_k\sigma_E}\sum\nolimits_{n,p}|\tilde{\psi}_n(p)|^2\exp\left[-\frac{(E-E_n)^2}{\sigma_E^2} - \frac{|k-p|^2}{\sigma_k^2}\right]$$

where $\tilde{\psi}_n(p)$ is the photonic eigenfunction in the reciprocal space given by the Fourier transform of the real-space eigenfunction $\psi_n(r)$. $\sigma_E$ and $\sigma_k$ denote additional broadenings in energy and wave vector to represent finite experimental resolution. The real-space dispersion is given by the real-space counterpart of the intensity distribution $I_M(E, k)$

$$I_R(E,x) = \frac{1}{\pi\sigma_E}\sum\nolimits_{n}|\psi_n(x)|^2\exp\left[-\frac{(E-E_n)^2}{\sigma_E^2}\right]$$

For our numerical simulation, we consider the following parameters: $m_X^x = 1.5\times10^{-5}m_e$, $m_X^y = 2.1\times10^{-5}m_e$, $m_Y^x = 2.2\times10^{-5}m_e$, and $m_Y^y = 1.5\times10^{-5}m_e$, where $m_e$ is the rest mass of an electron, $g_0$ = 120 meV, $E_{ex}$ = 2407 meV, $\Delta_X = -4$ meV, and $\Delta_Y = 4$ meV.

## Supplementary Materials

**This PDF file includes:**

Sections S1 to S9
Figs. S1 to S8
Table S1

## REFERENCES AND NOTES


1. M. Z. Hasan, C. L. Kane, Colloquium: Topological insulators. *Rev. Mod. Phys.* **82**, 3045–3067 (2010).
2. X.-L. Qi, S.-C. Zhang, Topological insulators and superconductors. *Rev. Mod. Phys.* **83**, 1057–1110 (2011).
3. K. V. Klitzing, G. Dorda, M. Pepper, New method for high-accuracy determination of the fine-structure constant based on quantized hall resistance. *Phys. Rev. Lett.* **45**, 494–497 (1980).
4. F. D. M. Haldane, S. Raghu, Possible realization of directional optical waveguides in photonic crystals with broken time-reversal symmetry. *Phys. Rev. Lett.* **100**, 013904 (2008).
5. Z. Wang, Y. Chong, J. D. Joannopoulos, M. Solja˘ić, Observation of unidirectional backscattering-immune topological electromagnetic states. *Nature* **461**, 772–775 (2009).
6. Z. Yang, F. Gao, X. Shi, X. Lin, Z. Gao, Y. Chong, B. Zhang, Topological acoustics. *Phys. Rev. Lett.* **114**, 114301 (2015).
7. R. Fleury, A. B. Khanikaev, A. Alù, Floquet topological insulators for sound. *Nat. Commun.* **7**, 11744 (2016).
8. R. Süsstrunk, S. D. Huber, Observation of phononic helical edge states in a mechanical topological insulator. *Science* **349**, 47–50 (2015).
9. M. C. Rechtsman, J. M. Zeuner, Y. Plotnik, Y. Lumer, D. Podolsky, F. Dreisow, S. Nolte, M. Segev, A. Szameit, Photonic Floquet topological insulators. *Nature* **496**, 196–200 (2013).

10. M. Hafezi, S. Mittal, J. Fan, A. Migdall, J. M. Taylor, Imaging topological edge states in silicon photonics. *Nat. Photonics* **7**, 1001–1005 (2013).
11. L. J. Maczewsky, J. M. Zeuner, S. Nolte, A. Szameit, Observation of photonic anomalous Floquet topological insulators. *Nat. Commun.* **8**, 13756 (2017).
12. L. Lu, Z. Wang, D. Ye, L. Ran, L. Fu, J. D. Joannopoulos, M. Solja˘ić, Experimental observation of Weyl points. *Science* **349**, 622–624 (2015).
13. J. Noh, S. Huang, D. Leykam, Y. D. Chong, K. P. Chen, M. C. Rechtsman, Experimental observation of optical Weyl points and Fermi arc-like surface states. *Nat. Phys.* **13**, 611–617 (2017).
14. Ş. K. Özdemir, S. Rotter, F. Nori, L. Yang, Parity–time symmetry and exceptional points in photonics. *Nat. Mater.* **18**, 783–798 (2019).
15. Y. Yang, Y. F. Xu, T. Xu, H. X. Wang, J. H. Jiang, X. Hu, Z. H. Hang, Visualization of a unidirectional electromagnetic waveguide using topological photonic crystals made of dielectric materials. *Phys. Rev. Lett.* **120**, 217401 (2018).
16. X.-T. He, E. T. Liang, J. J. Yuan, H. Y. Qiu, X. D. Chen, F. L. Zhao, J. W. Dong, A silicon-on-insulator slab for topological valley transport. *Nat. Commun.* **10**, 872 (2019).
17. B. Bahari, A. Ndao, F. Vallini, A. el Amili, Y. Fainman, B. Kanté, Nonreciprocal lasing in topological cavities of arbitrary geometries. *Science* **358**, 636–640 (2017).
18. M. A. Bandres, S. Wittek, G. Harari, M. Parto, J. Ren, M. Segev, D. N. Christodoulides, M. Khajavikhan, Topological insulator laser: Experiments. *Science* **359**, eaar4005 (2018).
19. Y. Zeng, U. Chattopadhyay, B. Zhu, B. Qiang, J. Li, Y. Jin, L. Li, A. G. Davies, E. H. Linfield, B. Zhang, Y. Chong, Q. J. Wang, Electrically pumped topological laser with valley edge modes. *Nature* **578**, 246–250 (2020).
20. H. Zhao, P. Miao, M. H. Teimourpour, S. Malzard, R. El-Ganainy, H. Schomerus, L. Feng, Topological hybrid silicon microlasers. *Nat. Commun.* **9**, 981 (2018).
21. S. Klembt, T. H. Harder, O. A. Egorov, K. Winkler, R. Ge, M. A. Bandres, M. Emmerling, L. Worschech, T. C. H. Liew, M. Segev, C. Schneider, S. Höfling, Exciton-polariton topological insulator. *Nature* **562**, 552–556 (2018).
22. P. St-Jean, V. Goblot, E. Galopin, A. Lemaître, T. Ozawa, L. le Gratiet, I. Sagnes, J. Bloch, A. Amo, Lasing in topological edge states of a one-dimensional lattice. *Nat. Photonics* **11**, 651–656 (2017).
23. W. Liu, Z. Ji, Y. Wang, G. Modi, M. Hwang, B. Zheng, V. J. Sorger, A. Pan, R. Agarwal, Generation of helical topological exciton-polaritons. *Science* **370**, 600–604 (2020).
24. J. Wu, S. Ghosh, R. Su, A. Fieramosca, T. C. H. Liew, Q. Xiong, Nonlinear parametric scattering of exciton polaritons in perovskite microcavities. *Nano Lett.* **21**, 3120–3126 (2021).
25. J. Wu, R. Su, A. Fieramosca, S. Ghosh, J. Zhao, T. C. H. Liew, Q. Xiong, Perovskite polariton parametric oscillator. *Adv. Photonics* **3**, 055003 (2021).
26. J. Kasprzak, M. Richard, S. Kundermann, A. Baas, P. Jeambrun, J. M. J. Keeling, F. M. Marchetti, M. H. Szymańska, R. André, J. L. Staehli, V. Savona, P. B. Littlewood, B. Deveaud, L. S. Dang, Bose–Einstein condensation of exciton polaritons. *Nature* **443**, 409–414 (2006).
27. L. Zhang, J. Hu, J. Wu, R. Su, Z. Chen, Q. Xiong, H. Deng, Recent developments on polariton lasers. *Prog. Quantum. Electron.* **83**, 100399 (2022).
28. S. Ghosh, R. Su, J. Zhao, A. Fieramosca, J. Wu, T. Li, Q. Zhang, F. Li, Z. Chen, T. Liew, D. Sanvitto, Q. Xiong, Microcavity exciton polaritons at room temperature. *Photonics Insights* **1**, R04 (2022).
29. R. Su, S. Ghosh, J. Wang, S. Liu, C. Diederichs, T. C. H. Liew, Q. Xiong, Observation of exciton polariton condensation in a perovskite lattice at room temperature. *Nat. Phys.* **16**, 301–306 (2020).
30. R. Su, S. Ghosh, T. C. H. Liew, Q. Xiong, Optical switching of topological phase in a perovskite polariton lattice. *Sci. Adv.* **7**, eabf8049 (2021).
31. M. Dusel, S. Betzold, O. A. Egorov, S. Klembt, J. Ohmer, U. Fischer, S. Höfling, C. Schneider, Room temperature organic exciton–polariton condensate in a lattice. *Nat. Commun.* **11**, 2863 (2020).
32. M. Dusel, S. Betzold, T. H. Harder, M. Emmerling, J. Beierlein, J. Ohmer, U. Fischer, R. Thomale, C. Schneider, S. Höfling, S. Klembt, Room-temperature topological polariton laser in an organic lattice. *Nano Lett.* **21**, 6398–6405 (2021).
33. Z. Song, Z. Fang, C. Fang, (d-2)-Dimensional edge states of rotation symmetry protected topological states. *Phys. Rev. Lett.* **119**, 246402 (2017).
34. J. Langbehn, Y. Peng, L. Trifunovic, F. von Oppen, P. W. Brouwer, Reflection-symmetric second-order topological insulators and superconductors. *Phys. Rev. Lett.* **119**, 246401 (2017).
35. M. Serra-Garcia, V. Peri, R. Süsstrunk, O. R. Bilal, T. Larsen, L. G. Villanueva, S. D. Huber, Observation of a phononic quadrupole topological insulator. *Nature* **555**, 342–345 (2018).
36. S. Imhof, C. Berger, F. Bayer, J. Brehm, L. W. Molenkamp, T. Kiessling, F. Schindler, C. H. Lee, M. Greiter, T. Neupert, R. Thomale, Topolectrical-circuit realization of topological corner modes. *Nat. Phys.* **14**, 925–929 (2018).
37. C. W. Peterson, W. A. Benalcazar, T. L. Hughes, G. Bahl, A quantized microwave quadrupole insulator with topologically protected corner states. *Nature* **555**, 346–350 (2018).
38. J. Noh, W. A. Benalcazar, S. Huang, M. J. Collins, K. P. Chen, T. L. Hughes, M. C. Rechtsman, Topological protection of photonic mid-gap defect modes. *Nat. Photonics* **12**, 408–415 (2018).
39. H. Xue, Y. Yang, F. Gao, Y. Chong, B. Zhang, Acoustic higher-order topological insulator on a kagome lattice. *Nat. Mater.* **18**, 108–112 (2019).
40. B.-Y. Xie, H. F. Wang, H. X. Wang, X. Y. Zhu, J. H. Jiang, M. H. Lu, Y. F. Chen, Second-order photonic topological insulator with corner states. *Phys. Rev. B* **98**, 205147 (2018).
41. X.-D. Chen, W. M. Deng, F. L. Shi, F. L. Zhao, M. Chen, J. W. Dong, Direct observation of corner states in second-order topological photonic crystal slabs. *Phys. Rev. Lett.* **122**, 233902 (2019).
42. A. El Hassan, F. K. Kunst, A. Moritz, G. Andler, E. J. Bergholtz, M. Bourennane, Corner states of light in photonic waveguides. *Nat. Photonics* **13**, 697–700 (2019).
43. A. Blanco-Redondo, B. Bell, D. Oren, B. J. Eggleton, M. Segev, Topological protection of biphoton states. *Science* **362**, 568–571 (2018).
44. W. Zhang, X. Xie, H. Hao, J. Dang, S. Xiao, S. Shi, H. Ni, Z. Niu, C. Wang, K. Jin, X. Zhang, X. Xu, Low-threshold topological nanolasers based on the second-order corner state. *Light Sci. Appl.* **9**, 109 (2020).
45. H.-R. Kim, M. S. Hwang, D. Smirnova, K. Y. Jeong, Y. Kivshar, H. G. Park, Multipolar lasing modes from topological corner states. *Nat. Commun.* **11**, 5758 (2020).
46. S. Mittal, V. V. Orre, G. Zhu, M. A. Gorlach, A. Poddubny, M. Hafezi, Photonic quadrupole topological phases. *Nat. Photonics* **13**, 692–696 (2019).
47. Y. Ota, F. Liu, R. Katsumi, K. Watanabe, K. Wakabayashi, Y. Arakawa, S. Iwamoto, Photonic crystal nanocavity based on a topological corner state. *Optica* **6**, 786–789 (2019).
48. R. Banerjee, S. Mandal, T. C. H. Liew, Coupling between exciton-polariton corner modes through edge states. *Phys. Rev. Lett.* **124**, 063901 (2020).
49. M. Li, D. Zhirihin, M. Gorlach, X. Ni, D. Filonov, A. Slobozhanyuk, A. Alù, A. B. Khanikaev, Higher-order topological states in photonic kagome crystals with long-range interactions. *Nat. Photonics* **14**, 89–94 (2020).
50. Z. Hu, D. Bongiovanni, D. Jukić, E. Jajtić, S. Xia, D. Song, J. Xu, R. Morandotti, H. Buljan, Z. Chen, Nonlinear control of photonic higher-order topological bound states in the continuum. *Light Sci. Appl.* **10**, 164 (2021).
51. N. A. Olekhno, A. D. Rozenblit, V. I. Kachin, A. A. Dmitriev, O. I. Burmistrov, P. S. Seregin, D. V. Zhirihin, M. A. Gorlach, Experimental realization of topological corner states in long-range-coupled electrical circuits. *Phys. Rev. B* **105**, L081107 (2022).
52. Q. Zhang, R. Su, X. Liu, J. Xing, T. C. Sum, Q. Xiong, High-quality whispering-gallery-mode lasing from cesium lead halide perovskite nanoplatelets. *Adv. Funct. Mater.* **26**, 6238–6245 (2016).



**Acknowledgment**

**Funding:** Q.X. acknowledges the National Natural Science Foundation of China (no. 12020101003 and no. 92250301) and the strong support from the State Key Laboratory of Low-Dimensional Quantum Physics and from the Tsinghua University Start-up Grant. R.S. and T.C.H.L. acknowledge support from the Singapore Ministry of Education via the AcRF Tier 3 Programme "Geometrical Quantum Materials" (MOE2018-T3-1-002). R.S. acknowledges support from the Nanyang Technological University via the Nanyang Assistant Professorship Start Up Grant. B.Z., H.S., and R.S. acknowledge the funding support from the Singapore National Research Foundation Competitive Research Program (grant no. NRF-CRP23-2019-0007). S.G. acknowledges funding support from the Excellent Young Scientists Fund Program (Overseas) of China and the National Natural Science Foundation of China (grant No. 12274034). J.W. acknowledges the Nano Letters Seed Grants. **Author contributions:** Q.X., R.S., and T.C.H.L. supervised the whole project. J.W. fabricated the device. R.S. and J.W. performed the experiments. S.G., S.M., T.C.H.L., and B.Z. performed the theoretical calculations. J.W., S.G., T.C.H.L., R.S., and Q.X. analyzed the data and wrote the manuscript, with input from all the authors. **Competing interests:** The authors declare that they have no competing interests. **Data and materials availability:** All data needed to evaluate the conclusions in the paper are present in the paper and/or the Supplementary Materials.

Submitted 23 December 2022
Accepted 20 April 2023
Published 24 May 2023
10.1126/sciadv.adg4322

ScienceAdvances

# Higher-order topological polariton corner state lasing

Jinqi Wu, Sanjib Ghosh, Yusong Gan, Ying Shi, Subhaskar Mandal, Handong Sun, Baile Zhang, Timothy C. H. Liew, Rui Su, and Qihua Xiong

*Sci. Adv.*, **9** (21), eadg4322.
DOI: 10.1126/sciadv.adg4322



*Science Advances* (ISSN ) is published by the American Association for the Advancement of Science. 1200 New York Avenue NW, Washington, DC 20005. The title *Science Advances* is a registered trademark of AAAS.